Linearization of Electrostatically Actuated Surface Micromachined 2-D Optical Scanner

Hiroshi Toshiyoshi, *Member, IEEE*, Wibool Piyawattanametha, Cheng-Ta Chan, and Ming C. Wu, *Member, IEEE*

***Abstract*—This paper presents an effective method of linearizing the electrostatic transfer characteristics of micromachined two–dimensional (2-D) scanners. The orthogonal scan angles of surface micromachined polysilicon scanner are controlled by using quadrant electrodes for electrostatic actuation. By using a pair of differential voltages over a bias voltage, we could improve the distortion of projected images from 72% to only 13%. A theoretical model has been developed to predict the angle-voltage transfer characteristics of the 2-D scanner. The simulation results agree very well with experimental data. Differential voltage operation has been found to suppress the crosstalk of two orthogonal scan axes by both experimentally and theoretically. We have found that a circular mirror is expected to have the lowest angular distortion compared with square mirrors. Perfect grid scanning pattern of small distortion (0.33%) has been successfully obtained by predistorting the driving voltages after calibration. [604]**

***Index Terms*—Electrostatic analysis, electrostatic force, microactuators, optical 2-D scanner, torsion mirror.**

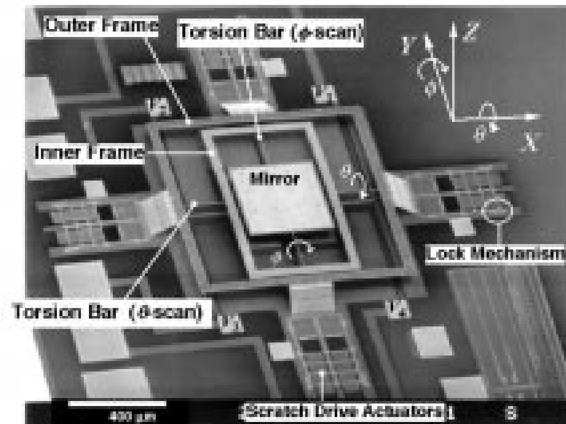

Fig. 1. SEM view of surface micromachined 2-D scanner. Quadrant electrodes underneath the mirror are used for electrostatic actuation.

I. Introduction

MICROMECHANICAL two-dimensional (2-D) optical scanners have attracted large attention because of their various microelectromechanical system (MEMS) applications such as free-space fiber-optic switches [1], [2], projection displays [3]–[7], confocal microscopes [8], [9], free-space laser communications [10], and laser radars. Electrostatic actuation offers many advantages for scanners, including fast response time and simple drive electronics rather than other methods. Electrostatic torsion mirrors can be actuated at low power consumption in both resonant and quasistatic operation. However, they have highly nonlinear transfer characteristics for converting applied voltage to rotation angle, which may result in, for instance, large distortion of projected images for displays, poor pointing accuracy for laser raders, and large insertion loss of fiber-optic switches. Therefore, such applications use complex feedback control system.

A pair of one-dimensional (1-D) scanners can be cascaded to compose a 2-D scanner [1], [5], [6]. The advantage of this architecture is that the orthogonal scan angles can be independently controlled with two driving voltages. However, the field of view is limited by the size of the second mirror; the light spot projected onto the second mirror might walk off when the scan angle of the first mirror is large. On the other hand, 2-D scanners made of a single micromirror do not have such walk-off problem [2], [5], [12]. Difficulty of this approach, however, lies in the crosstalk of driving voltages for 2-D scanning in addition to the electrostatic nonlinearity.

In this paper, we present a linearization scheme that effectively suppresses the nonlinearity of the electrostatic 2-D scanners by using differential voltage operation. The differential voltage operation also suppresses the crosstalk between the scan axes. A theoretical model has been developed to predict the angle-voltage transfer function of 2-D scanner. The simulation results agree very well with experimental data. We have studied the effect of mirror shape on the linearity of the scan angle and found that a circular mirror has the lowest angular distortion compared with square mirrors. We have also demonstrated scanning an almost perfect grid pattern by predistorting the driving voltages after calibrating the 2-D scanner. Although this technique is not able to eliminate feedback control in applications such as free-space fiber-optic switches, it would be useful to simplify the design of feedback control system.

II. Electromechanical Simulation Model

Fig. 1 shows the scanning electron micrograph (SEM) of the 2-D scanner used for our simulation and experiment. It is fabricated by surface-micromachining foundry service (Multi-User MEMS Process, or MUMPs, by Cronos Integrated Microsystems, Research Triangle Park, NC). The structure is made of polysilicon, and the micromirror surface is coated with gold for higher reflectivity. The mirror plate (400 μm $\times$ 400 μm in area and 1.5 μm in thickness) is suspended by the double-gimbal structure, which consists of two pairs of

Manuscript received July 26, 2000; revised January 23, 2001. This work was supported in part by DARPA (DAAH 01-99-C-R220). Subject Editor T. Kenny.

The authors are with Department of Electrical Engineering, University of California, Los Angeles, CA 90032 USA (e-mail: wu@icsl.ucla.edu).

Publisher Item Identifier S 1057-7157(01)03940-3.

1057–7157/01$10.00 © 2001 IEEE

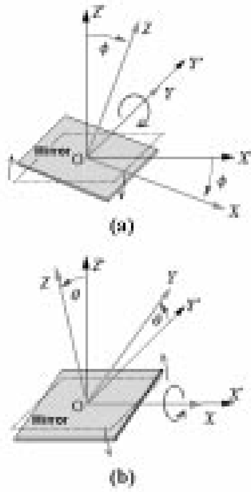

Fig. 2. Coordinate conversion around (a) the Y-axis and (b) X-axis. Frame XYZ rotates with the mirror, and the coordinate is measured in the new frame, $X'Y'Z'$.

torsion bars (2 μm wide, 1.5 μm thick, and 200 μm long) for ϕ- and θ-scan. To achieve large scan angle, the micromirror is suspended above the substrate with an air gap of 72 μm using the micro-elevator self-assembly (MESA) technique [11]. Four sets of scratch-drive actuators [12] are used to push up the frame structure until it is locked by the small springs. The suspended structure is electrically grounded, and the scan angles are electrostatically controlled by using four voltages (V_1, V_2, V_3, V_4) applied to the quadrant electrodes underneath the mirror. Incident light is aligned to shoot the center of the micromirror, and the reflection light is spatially modulated by the motion of the mirror. As shown in the figure, we take scan angles θ and ϕ around the X- and Y-axis, respectively.

We model the mirror by using coordinate conversion illustrated in Fig. 2. The origin of frame XYZ is set at the center of the mirror. We rotate the frame with the mirror around the Y-axis by angle ϕ, as shown in Fig. 2(a), leaving a new frame $X'Y'Z'$ at the initial place. The new coordinate (x', y', z') measured in frame $X'Y'Z'$ after rotation is written by using a transfer matrix as

$$\begin{pmatrix} x' \\ y' \\ z' \end{pmatrix} = \mathbf{M}_\phi \begin{pmatrix} x \\ y \\ z \end{pmatrix}, \qquad \mathbf{M}_\phi = \begin{pmatrix} \cos\phi & 0 & \sin\phi \\ 0 & 1 & 0 \\ -\sin\phi & 0 & \cos\phi \end{pmatrix} \tag{1}$$

where (x, y, z) is the coordinate of the identical point measured in frame XYZ. For θ-scan around the X-axis, we similarly write the coordinate transfer as

$$\begin{pmatrix} x' \\ y' \\ z' \end{pmatrix} = \mathbf{M}_\theta \begin{pmatrix} x \\ y \\ z \end{pmatrix}, \qquad \mathbf{M}_\theta = \begin{pmatrix} 1 & 0 & 0 \\ 0 & \cos\theta & -\sin\theta \\ 0 & \sin\theta & \cos\theta \end{pmatrix}. \tag{2}$$

Our model applies ϕ-scan before θ-scan, because the rotating axis of ϕ-scan moves with the inner frame when the frame is rotated in the θ-direction (see Fig. 1). The transfer matrix for this cascaded operation is

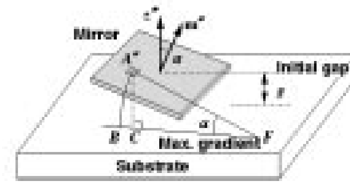

Fig. 3. Schematic mirror after two rotations. Maximum slope angle α is equal to the angle between the normal vector $\mathbf{m}''$ and the Z''-axis.

$$\begin{aligned} \mathbf{M}_{\theta\phi} &= \mathbf{M}_\theta \mathbf{M}_\phi \\ &= \begin{pmatrix} 1 & 0 & 0 \\ 0 & \cos\theta & -\sin\theta \\ 0 & \sin\theta & \cos\theta \end{pmatrix} \begin{pmatrix} \cos\phi & 0 & \sin\phi \\ 0 & 1 & 0 \\ -\sin\phi & 0 & \cos\phi \end{pmatrix} \\ &= \begin{pmatrix} \cos\phi & 0 & \sin\phi \\ \sin\theta\sin\phi & \cos\theta & -\sin\theta\cos\phi \\ -\cos\theta\sin\phi & \sin\theta & \cos\theta\cos\phi \end{pmatrix}. \end{aligned} \tag{3}$$

The matrix can be used for transferring points as well as vectors. An element of small area (dS) on the mirror, $A = (x, y, 0)$, and the normal vector of the mirror, $\mathbf{m} = (0, 0, 1)$, are transferred to

$$\begin{aligned} A'' = &(x\cos\phi,\ x\sin\theta\sin\phi + y\cos\theta, \\ &-x\cos\theta\sin\phi + y\sin\theta) \end{aligned} \tag{4}$$

and

$$\mathbf{m}'' = (\sin\phi,\ -\sin\theta\cos\phi,\ \cos\theta\cos\phi) \tag{5}$$

respectively. Note that these coordinates after two conversions are now measured in the new frame, $X''Y''Z''$, whose X''- and Y''-axes are in parallel with the torsion bars at the initial position.

As illustrated in Fig. 3, the maximum slope angle of the mirror to the substrate, α, is equal to the angle between the Z''-axis ($\mathbf{z}'' = (0, 0, 1)$), and the normal vector of the mirror, $\mathbf{m}''$. Therefore, we take the inner product of them to find α as follows:

$$\begin{aligned} \mathbf{m}'' \cdot \mathbf{z}'' &= \cos\alpha, \qquad (|\mathbf{m}''| = |\mathbf{z}''| = 1) \\ &= \cos\theta\cos\phi \end{aligned} \tag{6}$$

$$\alpha(\theta, \phi) = \cos^{-1}(\cos\theta\cos\phi). \tag{7}$$

Taking point C on the substrate straight down from point A'', we write the length $\overline{A''C}$ as $g - z + A''_z$, where g is the initial gap between the mirror and the substrate, z is the vertical displacement of the mirror center in $-Z''$ direction, and A''_z is the Z''-component of coordinate A'' [see (4)]. Assuming that the flux of electric field on element A'' is represented by arc $\overset{\frown}{A''B}$, we write the strength of the field by dividing the applied voltage V by the length of the arc. The arc length is calculated to be

$$\overset{\frown}{A''B} = \overline{A''F} \cdot \alpha = \frac{\overline{A''C}}{\sin\alpha} \cdot \alpha. \tag{8}$$

Therefore, the electric field E is

$$\begin{aligned} E &= \frac{\mathrm{V}}{\widehat{A''B}} \\ &= \frac{\mathrm{V}}{\dfrac{g+A''_z}{\sin\alpha}\cdot\alpha} \\ &= \frac{\sin\alpha}{\alpha}\cdot\frac{\mathrm{V}}{g-z-x\cos\theta\sin\phi+y\sin\theta}. \end{aligned} \tag{9}$$

The electrostatic force acting on this element is written as

$$\begin{aligned} dP &= \tfrac{1}{2}\,\varepsilon_0 E^2\,dS \\ &= \frac{1}{2}\,\varepsilon_0\left(\frac{\sin\alpha}{\alpha}\cdot\frac{1}{g-z-x\cos\theta\sin\phi+y\sin\theta}\right)^2 V^2\,dS \end{aligned} \tag{10}$$

where ε_0 is the dielectric constant of vacuum, 8.85×10^{-12} F/m, and $dS(=dx\cdot dy)$ is the area of the element. Neglecting the fringing effect of the electric field, we estimate the electrostatic torque by numerically integrating the force dP over the portion of the mirror that corresponds to the electrode. Hence, the electrostatic torques for ϕ- and θ-scan are

$$T_\phi^E(V) = \tfrac{1}{2}\,\varepsilon_0 V^2 \iint_S x \cdot\left(\frac{\sin\alpha}{\alpha}\cdot\frac{1}{g-x\cos\theta\sin\phi+y\sin\theta}\right)^2 dS, \tag{11a}$$

$$T_\theta^E(V) = \tfrac{1}{2}\,\varepsilon_0 V^2 \iint_S (-y) \cdot\left(\frac{\sin\alpha}{\alpha}\cdot\frac{1}{g-x\cos\theta\sin\phi+y\sin\theta}\right)^2 dS \tag{11b}$$

respectively. The negative sign of $(-y)$ in the second equation is due to the direction of angle θ defined with respect to the coordinate (Fig. 2).

While the mirror is rotated by the torques around the X- and Y-axes, it is also pulled down along $-Z$ direction. The Z-component of the electrostatic force dP (10) is written as $dP\cos\alpha$. Hence, the electrostatic force is

$$F_Z^E(V) = \tfrac{1}{2}\,\varepsilon_0 V^2 \iint_S \cos\phi\cos\theta \cdot\left(\frac{\sin\alpha}{\alpha}\cdot\frac{1}{g-x\cos\theta\sin\phi+y\sin\theta}\right)^2 dS. \tag{11c}$$

Since the mirror is controlled by the quadrant electrodes, $(\mathrm{V}_1, \mathrm{V}_2, \mathrm{V}_3, \mathrm{V}_4)$, the total electrostatic torques and force are obtained by adding four contributing terms as

$$T_\phi^E = \sum_{i=1}^{4} T_\phi^E(\mathrm{V}_i), \tag{12a}$$

$$T_\theta^E = \sum_{i=1}^{4} T_\theta^E(\mathrm{V}_i), \tag{12b}$$

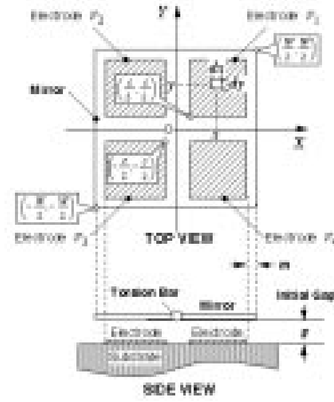

Fig. 4. Arrangement of quadrant electrodes and a square mirror. Electrostatic force in the hatched area is integrated to calculate electrostatic torque around the torsion bar.

$$F_Z^E = \sum_{i=1}^{4} F_Z^E(\mathrm{V}_i). \tag{12c}$$

Each term has different range of integration the electrostatic force. For a square mirror and quadrant electrodes used in our experiment, we modeled the dimensions as illustrated in Fig. 4. Four electrodes are located underneath the mirror, and their center is precisely aligned to that of the mirror by the MESA technique. In order to avoid electric short circuit upon contact, the mirror size $W(=400\mu\mathrm{m})$ is designed to be slightly larger than the electrodes by margin $m(=30\ \mu\mathrm{m})$, and there is a gap $c(=20\ \mu\mathrm{m})$ between the tiled electrodes. Since we have assumed that electrostatic attraction force is distributed all over the mirror, we took $[0\le x\le W/2,\ 0\le y\le W/2]$ as a range of integration for the first quadrant electrode (V_1) for simplicity. Equations (11a), (11b), and (11c) are applicable to mirrors of arbitrary shapes by modifying the range of integration. Mirror-shape dependence of scanning linearity will be discussed later.

On the other hand, mechanical restoring torques of the torsion bars are written in a linear term of angle as [13]

$$T_\phi^M = 2\frac{Gwt^3}{3l}\,\phi\left(1-\frac{192}{\pi^5}\,\frac{t}{w}\tanh\frac{\pi w}{2t}\right), \tag{13a}$$

$$T_\theta^M = 2\frac{Gwt^3}{3l}\,\theta\left(1-\frac{192}{\pi^5}\,\frac{t}{w}\tanh\frac{\pi w}{2t}\right) \tag{13b}$$

where G is the modulus of rigidity, and w, l, and t are the width, length, and thickness of the torsion bar, respectively. We used a constant value of 73 GPa for G since silicon is known to have a linear stress-strain characteristic before mechanical fracture [14], and that our device operates in the range lower than the yield strength.

The suspensions experience torsion as well as bending due to the electrostatic attraction force. For the mechanical restoring force in the Z''-direction, we used a fixed-fixed beam model for the suspensions (total length of $2l$) [15].

$$F_Z^M = \frac{1}{2}\cdot\frac{192EI}{(2l)^2}\,z \tag{13c}$$

where E is Young's modulus (190 GPa for silicon), and $I(=wt^3/12)$ is the suspension's moment of inertia of area. Since two fixed-fixed beams are cascaded in the double gimbal structure, we have a factor of 1/2 in (13c). Strictly speaking, these mechanical torques and force should be coupled each other. In particular, stiffness of bending beam in the Z''-direction changes with the twisting angle of the beam because the neutral plane of the beam deviates from the initial neutral plane, resulting in the change of moment of inertia of area. In our experiment, however, maximum torsion angle was as small as 1 degree and maximum deflection of beam was no greater than 2% of its length. Therefore, we used a linear model (13c) for the bending beams, which was regarded as independent of the torsional motion. In addition, deformation of gimbal frame is not taken into account. For more detail analysis, one should use finite element method.

One can find values of (ϕ, θ, z) under electromechanical equilibrium condition by numerically solving the following simultaneous equations:

$$\begin{cases} T_\phi^E = T_\phi^M, \\ T_\theta^E = T_\theta^M, \\ F_Z^E = F_Z^M. \end{cases} \tag{14}$$

We used Mathcad (Mathsoft, Inc., Cambridge, MA) to numerically find solutions of ϕ and θ as a function of voltages.

Using four independent voltages makes the control system complicated. Hence we use only two independent parameters V_x and V_y to control ϕ and θ, respectively. One of the possible voltage combinations to tilt the mirror toward the fourth quadrant electrode (corresponding to $\phi \geq 0$ and $\theta \geq 0$) is

$$\begin{cases} \mathrm{V}_1 = V_x, \\ \mathrm{V}_2 = 0, \\ \mathrm{V}_3 = \mathrm{V}_y, \\ \mathrm{V}_4 = \mathrm{V}_x + \mathrm{V}_y. \end{cases} \tag{15}$$

We call this scheme as "nondifferential" drive. Note that two voltages are superposed for V_4 and that V_2 is grounded as a reference electrode. In Fig. 5, we show the results of simulated angles, ϕ and θ as a function of V_x and V_y. It is observed that angle ϕ and θ increase with increasing V_x and V_y, and that the crosstalk is too large to achieve independent control of ϕ and θ. Furthermore, they have large nonlinearity, which possibly distorts the shape of scanned image.

By sequentially shifting those voltage components, the mirror can be tilted to each electrode. After obtaining similar plots of ϕ and θ for each quarter, we put them together to show the entire angle-voltage characteristics in a single plot, as shown in Fig. 6(a) and (b). Deviation from the ideal characteristic surface (indicated by dashed lines) is large when V_x and V_y are set to large values. Again, note that the voltage combinations are different in each quadrant section and that V_x and V_y take positive values only. Circled numbers in Figs. 5 and 6 are to make correspondence to the scanned image to be shown in Fig. 9 later.

In addition to rotational motions, the mirror is attracted downward in the Z-direction due to the finite stiffness of the suspension as shown in Fig. 6(c). The change in the electrostatic gap

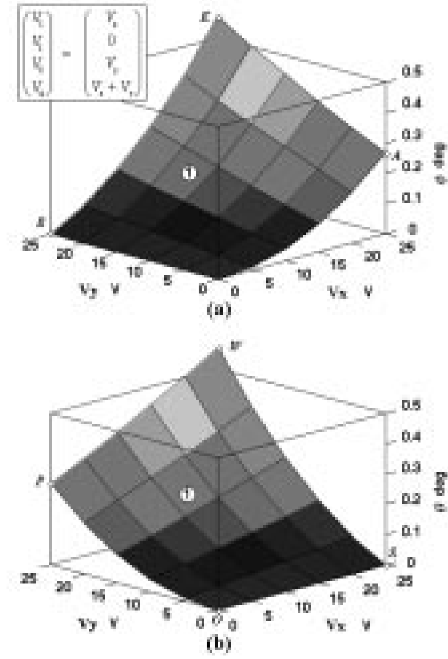

Fig. 5. Simulated mirror angles ϕ and θ as a function of voltages V_x and V_y to draw the first quadrant on the screen. Voltages (inset) are applied without bias voltage.

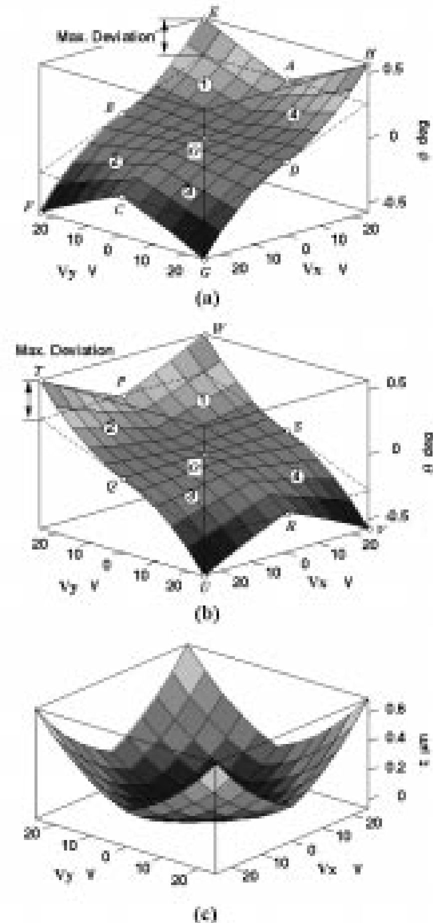

Fig. 6. Simulated results of angle-voltage characteristics of the 2-D scanner by nondifferential drive. Dashed lines define the ideal characteristic plane.

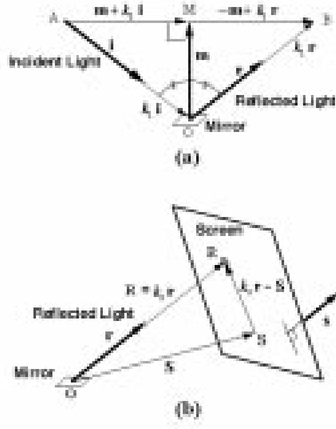

Fig. 7. Theoretical models of (a) reflection and (b) projection.

also has an effect to enhance the electrostatic torque. However, the maximum vertical displacement is small (0.8 μm) compared with the initial air gap (72 μm), and the effect is not significant here. We will come back to this point later when we discuss the differential voltage operation.

III. Optical Simulation Model

In this section, we discuss a simulation model to relate the mirror's normal vector to the direction of reflected light. As depicted in Fig. 7(a), an incident light vector $\mathbf{i}$, a reflected light vector $\mathbf{r}$, and the normal vector of the mirror $\mathbf{m}$ lie in the identical plane, and the incident angle is equal to reflection angle. A pair of congruent triangles AMO and BMO are found by using points A, B, and, M on the extensions of unit vectors $\mathbf{i}$, $\mathbf{r}$, and $\mathbf{m}$, respectively. Since $\overrightarrow{AO}$ is in parallel with $\mathbf{i}$, it is written as $k_1\mathbf{i}$, where k_1 is a scalar. As vector $\overrightarrow{OM}$ is perpendicular to vector $\overrightarrow{AM}$, their inner product is zero:

$$\overrightarrow{OM} \cdot \overrightarrow{AM} = \mathbf{m} \cdot (\mathbf{m} + k_1\mathbf{i}) = 0. \tag{16}$$

Therefore, we find $k_1 = -1/(\mathbf{m} \cdot \mathbf{i})$. The same value of k_1 is also used to represent vector $\overrightarrow{OB}$ as $k_1\mathbf{r}$. Since vector $\overrightarrow{AM}$ is equal to $\overrightarrow{MB}$, we find $\mathbf{r}$ as

$$\begin{aligned} \mathbf{m} + k_1\mathbf{i} &= -\mathbf{m} + k_1\mathbf{r}, \\ \mathbf{r} &= \mathbf{i} + \frac{2}{k_1}\mathbf{m}. \end{aligned} \tag{17}$$

Substituting the value of k_1 into (17), we obtain an expression of $\mathbf{r}$ as a function of $\mathbf{i}$ and $\mathbf{m}$:

$$\mathbf{r} = \mathbf{i} - 2(\mathbf{i} \cdot \mathbf{m})\mathbf{m}. \tag{18}$$

The first term shows that the vector components parallel to the mirror surface are preserved, and the second term implies that optical scan angle is not always twice as much as the mechanical scan angle but that the leverage factor is modulated by the incident angle to the mirror. This nonlinear effect is intrinsic to reflection and cannot be eliminated by changing the design of the scanner.

Next step is to find a projected spot on a screen. As illustrated in Fig. 7(b), we place a screen at S, where vector $\overrightarrow{OS}$ is identified as vector $\mathbf{S}$, and the normal vector of the screen is $\mathbf{s}$. Since a projected spot R can be found on the extension of vector $\mathbf{r}$, we write $\overrightarrow{OR}$ as $k_2\mathbf{r}$, where k_2 is a scalar. Vector $\overrightarrow{SR}(=k_2\mathbf{r} - \mathbf{S})$ lies in the screen and it is perpendicular to $\mathbf{s}$, and thus their inner product is zero. Hence, we find $k_2 = (\mathbf{S} \cdot \mathbf{s})/(\mathbf{r} \cdot \mathbf{s})$. The projected light spot is, therefore, located at

$$\mathbf{R} = \left(\frac{\mathbf{S} \cdot \mathbf{s}}{\mathbf{r} \cdot \mathbf{s}}\right)\mathbf{r}. \tag{19}$$

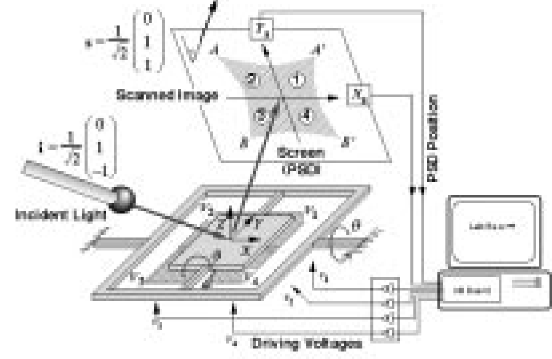

Fig. 8. Schematic illustration showing the setup of the 2-D scanner, the screen, and the direction of the incident light.

Fig. 8 schematically illustrates the set up of our optical scanning experiment. The incident light from a laser diode (Newport, model 700P, $\lambda = 633$ nm) is guided with a multimode fiber with a ball-lens along $(1/\sqrt{2})(0,\,1,\,-1)$ direction, and is collimated to the mirror from a 3-mm distance. A position sensitive detector (PSD, ON-TRAK Photonics Inc., model OT-3210), which serves as a screen, is located 3 cm from the mirror with its normal vector in $(1/\sqrt{2})(0,\,1,\,1)$ direction. Driving voltages are PC-controlled with an I/O card (PCI-MIO-16XE-10) and LabView (both from National Instruments Corp., Austin, TX) through our home made 4-channel voltage amplifiers (using hybride operation amplifiers, APEX PA85A). The position data $(X_S,\,Y_S)$ from the PSD is acquired by the same LabView program.

In (19), the light spot is measured in the coordinate whose origin is located at the center of the mirror. To read it by using the X_SY_S-axes on the screen (PSD), we need to apply another transfer matrix. When the screen is set with its normal vector along $(1/\sqrt{2})(0,\,1,\,1)$ direction, as shown in Fig. 8, the X_SY_S-plane can be in parallel with the XY-plane (of frame XYZ) after rotating the X_SY_S-plane by 135° in $-\theta$ direction. The new coordinate measured on the screen is

$$\begin{aligned} \mathbf{R}_S &= \mathbf{M}_\theta|_{\theta=-135^\circ}\mathbf{R} \\ &= \frac{1}{\sqrt{2}}\begin{pmatrix} 1 & 0 & 0 \\ 0 & -1 & 1 \\ 0 & -1 & -1 \end{pmatrix}\begin{pmatrix} R_x \\ R_y \\ R_z \end{pmatrix} \\ &= \begin{pmatrix} R_x \\ -\frac{1}{\sqrt{2}}(R_y - R_z) \\ -\frac{1}{\sqrt{2}}(R_y + R_z) \end{pmatrix}. \end{aligned} \tag{20}$$

We take the X- and Y-components of this vector to locate the spot on the screen.

Fig. 9(a) plot the simulated projection image of the 2-D scanner operated by the control voltage shown by (15). Voltages

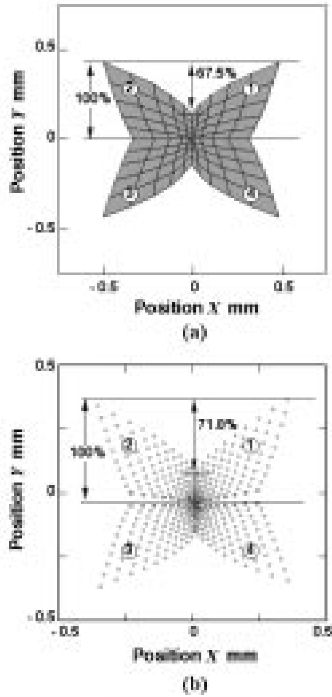

Fig. 9. (a) Simulated scan image by nondifferential drive and (b) experimental result (corresponding to Fig. 6).

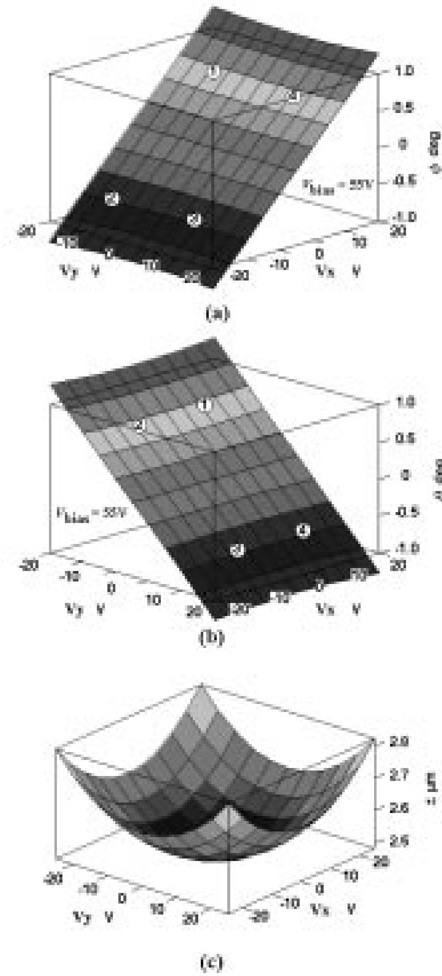

Fig. 10. Simulated angles as a function of differential voltages around a bias voltage of 55 V.

have been changed from 0 V to 34 V for V_x and from 0 V to 17 V for V_y in each quadrant. Larger driving voltages are needed for V_x rather than V_y in order to equalize the scan range in both X_S and Y_S on the screen due to the angled incidence. Because of the nonlinear electrostatic characteristics, the image is skewed toward the corners by as much as 67.5% of the half scan range. Each quadrant section marked up with a circled number corresponds to that in the angle-voltage plot in Fig. 6. The simulation results agree very well with the experimental data shown in Fig. 9(b); the maximum distortion was measured to be 71.8%. The distortion near $Y = 0$ is due to the hysteresis of electrostatic operation. The scan area has been calculated to be larger than that of experiment because we have overestimated the electrostatic force by neglecting the effect of the substrate as a ground plane.

IV. Linearization by Differential Voltage Operation

Applying a small control voltage over a large bias voltage has been known to improve the linearity in the limited range of 1-D electrostatic actuators whose output is governed by the square of voltage [16]. It has been also known that differential drive with bias voltage can further improve the linearity of 1-D comb drive actuator of lateral motion [17] and 1-D torsion mirror [18]. However, behavior of 2-D-torsion mirror has not been fully understood because of the complexity in describing electrostatic force as a function of rotational angles and vertical translation of the mirror. To our knowledge, the present paper is the first theoretical and experimental demonstration of the linearization and crosstalk suppression of 2-D scanners based on the torsion mirror structure.

We use two independent differential voltages, V_x and V_u, over a bias voltage, $\mathrm{V}_{\mathrm{bias}}$, to apply the driving voltages as follows:

$$\begin{cases} \mathrm{V}_1 = \mathrm{V}_{\mathrm{bias}} + \frac{\mathrm{V}_x + \mathrm{V}_y}{2} \\ \mathrm{V}_2 = \mathrm{V}_{\mathrm{bias}} + \frac{-\mathrm{V}_x + \mathrm{V}_y}{2} \\ \mathrm{V}_3 = \mathrm{V}_{\mathrm{bias}} + \frac{-\mathrm{V}_x - \mathrm{V}_y}{2} \\ \mathrm{V}_4 = \mathrm{V}_{\mathrm{bias}} + \frac{\mathrm{V}_x - \mathrm{V}_y}{2} \end{cases} \tag{21}$$

where V_x and V_y are chosen such that $\mathrm{V}_i \geq 0 (i = 1, 2, 3, 4)$. Simulated scan angles as a function of differential voltages are shown in Fig. 10. In this calculation, we set bias voltage at 55 V and changed differential voltages from -20 V to 20 V with an increment of 4 V. Different from the results of nondifferential operation (Fig. 6), the characteristic surfaces are not warped. Furthermore, the voltage crosstalk is negligible except near the corners. With the same setup illustrated in Fig. 8, we calculated the scanned image as shown in Fig. 11(a). The maximum distortion has been suppressed down to 17.1%. Scan width at the top, $A - A'$, is slightly different from that at the bottom, $B - B'$, as

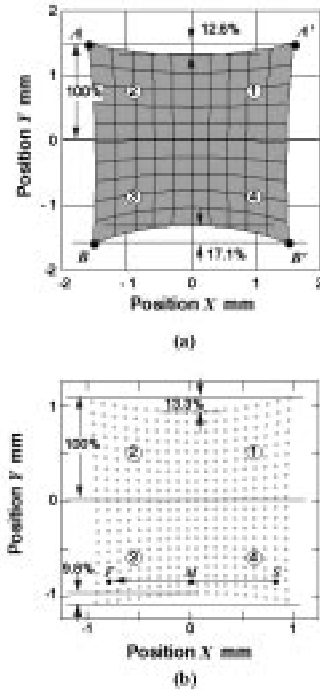

Fig. 11. (a) Simulated scan image by differential operation and (b) experimental result.

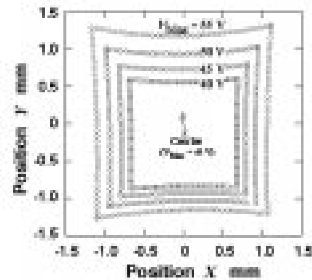

Fig. 12. Experimental results of various scan field at biasing voltages from 40 V to 55 V.

predicted by the second term of (18). The simulation data agrees well with the experimental data shown in Fig. 11(b). The distortion is large (13.3%) at the top and small (9.8%) at the bottom. This small mismatch is due to the imperfection of optical alignment in our experiment.

Fig. 12 shows the scan field experimentally obtained by the differential voltages between -34 V and 34 V for V_x and from -17 V to 17 V for V_y over bias voltages of 40, 45, 50 and 55 V. The scan range can be tuned linearly with the bias voltage. At the same time, the field was found to drift toward $+Y$ as the bias voltage increases. This result implies that the structure of the scanner is not perfectly symmetric but it has a small initial offset angle. The offset causes unbalance of electrostatic torque across the torsion bars, and the mirror starts tilting in that direction when the bias voltages are increased. At bias voltages over 60 V, the mirror becomes unstable due to electrostatic pull-in. For this reason, we have chosen small scan range (corresponding to the mirror angle of less than 2°) to avoid damaging the mirror.

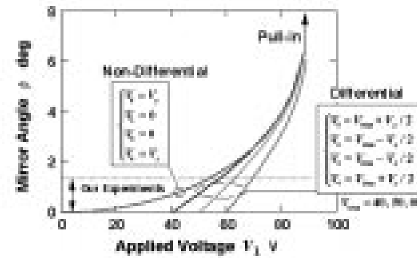

Fig. 13. Simulated angle ϕ-voltage V_1 curves at different bias voltages (40, 50, and 60 V).

Here arises a question regarding the effect on the stable deflection range when changing driving scheme from nondifferential to differential. For simplicity, we used our analytical model for 1-D simulation in the ϕ direction only. For nondifferential operation, we applied voltage V_x to V_1 and V_4, leaving V_2 and V_3 grounded. On the other hand, voltages described in (21) were used for differential operation but with V_y forced to zero. Fig. 13 compares the angle ϕ as a function of voltage V_1. It has been found that pull-in angle slightly decreases with increasing bias voltage but the shift is negligible for our scanner. The influence of bias voltage on the pull-in angle becomes significant when the initial air gap becomes small compared with the mirror size.

V. Mirror Shape Dependence of Linearity

We briefly investigate the mechanism of linearization by simplifying the model back into a 1-D torsion mirror. Equation (11) indicates that the square of voltage is explicitly included in the electrostatic torque. When applying a differential voltage, $\mathrm{V_{diff}}$, over a bias voltage, $\mathrm{V_{bias}}$, we write electrostatic torque acting on the left-hand side of the mirror as $G_L(\mathrm{V_{bias}} - \mathrm{V_{diff}}/2)^2$ and that on the right-hand side as $G_R(\mathrm{V_{bias}} + \mathrm{V_{diff}}/2)^2$, where G_L and G_R are geometrical factors $(G_R \cdot G_L < 0)$. The net electrostatic torque is

$$\begin{aligned} T_{\mathrm{NET}}^{E} &= G_L\left(\mathrm{V_{bias}} - \frac{\mathrm{V_{diff}}}{2}\right)^2 + G_R\left(\mathrm{V_{bias}} + \frac{\mathrm{V_{diff}}}{2}\right)^2 \\ &= (G_R - G_L)\mathrm{V_{bias}}\mathrm{V_{diff}} + (G_R + G_L)\left(\mathrm{V_{bias}^2} + \frac{\mathrm{V_{diff}^2}}{4}\right). \end{aligned} \tag{22}$$

This equation is true to most 1-D electrostatic actuators that do not change the shape of the air gap so much. In the case of parallel-plate actuator, for example, the geometrical factors, G_L and G_R, are constants of the same value with opposite signs. Hence, the second term is cancelled out, leaving the first term, which is proportional to $\mathrm{V_{diff}}$. On the other hand, the process of linearization is different for torsion mirrors because G_L and G_R are actually functions of $\mathrm{V_{diff}}$ and that the second term remains. However, our numerical calculation has found that the second term is also proportional to $\mathrm{V_{diff}}$ when appropriate values of voltages are used (at least $|\mathrm{V_{diff}}| \leq 2\mathrm{V_{bias}}$). Hence, the net torque of the 1-D scanner is also proportional to $\mathrm{V_{diff}}$. Similar mechanism of linearization has been found in the differential operation of the 2-D scanner by using the theoretical model. As we have seen in Fig. 10, each scan angle has been linearized to

one of the two control voltages; at the same time, the crosstalk between these voltages has been also significantly suppressed.

For this reason, the linearity of 2-D scanner depends on the geometrical factor, that is, the shape of the mirror. As shown in Figs. 6 and 10, the angular distortion becomes large near the corners, where the mirror is diagonally titled toward one of the electrodes. Therefore, the linearity would be improved if the extra attraction force is reduced by chopping off the corners of the mirror.

We used our theoretical model to compare the distortion of three different types of mirrors: square (control), diamond shape, and circular mirrors. We set the mirror dimensions such that a beam spot of the same diameter ($W = 400$ μm) can be fit in the mirrors: the square and diamond mirrors are $W \times W$ in area, while the circular one is W in diameter. Fig. 14 compares the relative angular distortion as a function of mirror angles ϕ and θ. Driving voltages has been set at large values (V_x, $\mathrm{V}_y = -40 \sim 40$ V and $\mathrm{V}_{\mathrm{bias}} = 55$ V) to clearly show the difference of distortion at a large scan range. Since the distortion of projected image depends on the attitude of the screen, we used the mechanical angle of the scanner for comparison. The distortion referred in this paper is defined by the angle deviation from the ideal value and is normalized by the maximum scan angle; see the dashed lines in Fig. 6 as an example of the ideal plane (which is indistinguishable in Fig. 10). The square mirror and the diamond shape mirror have been calculated to have large angular distortion of more than 5% at the corners ($\phi = \theta = 1.5°$) while the circular one has 2.6%.

We have fabricated scanners of square and circular mirrors over the identical electrode design (Fig. 4) to experimentally compare distortion. After carefully aligning the optics (Fig. 8) and minimizing the image distortion for each mirror, we adjusted differential driving voltages to have equivalent size of projected images ($-1.5° \leq \phi \leq 1.5°$, $-1.5° \leq \theta \leq 1.5°$) at the same bias voltage. As a result, we found that the circular mirror had smaller image distortion (3.1% on PSD) rather than the square one (5.6% on PSD) in the scan range less than 1.5°.

VI. Calibration for Higher Pointing Accuracy

Transfer function of 2-D scanner is a mapping from four voltages, (V_1, V_2, V_3, V_4), to two angles when voltages are controlled independently. To solve the inverse problem, therefore, one needs to look for four unknown voltages from two given angles but may find more than one solution. On the other hand, differential drive allows us to find a unique combination of voltages, (V_x, V_y), from two given angles, (ϕ, θ), and one given bias voltage, $\mathrm{V}_{\mathrm{bias}}$.

Here we demonstrate highly accurate positioning of 2-D scanner by predistorting the differential driving voltages after calibrating the electrostatic characteristics of the scanner. First, we prepare look-up tables of continuous transfer functions, $X_S(\mathrm{V}_x, \mathrm{V}_y)$ and $Y_S(\mathrm{V}_x, \mathrm{V}_y)$, by numerically interpolating the data shown in Fig. 11(a) by using software. We then convert the target coordinates, (X_S, Y_S), back into corresponding driving voltages V_x and V_y by using the Newton's method on the look-up table. For example, Fig. 15(a) shows voltages

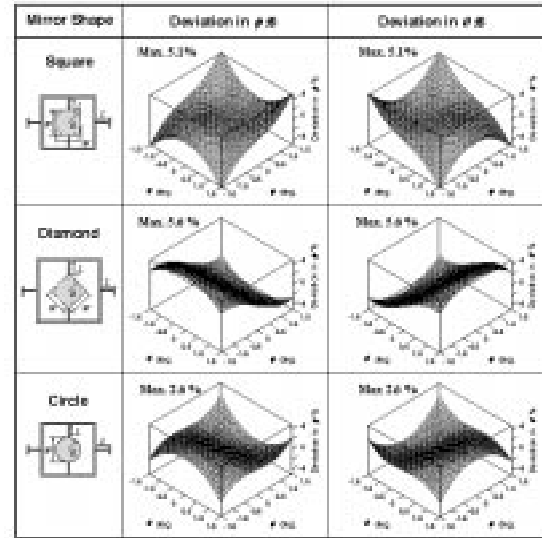

Fig. 14. Simulated angular distortion of three types of scanners: square, diamond-shape, and circular mirrors.

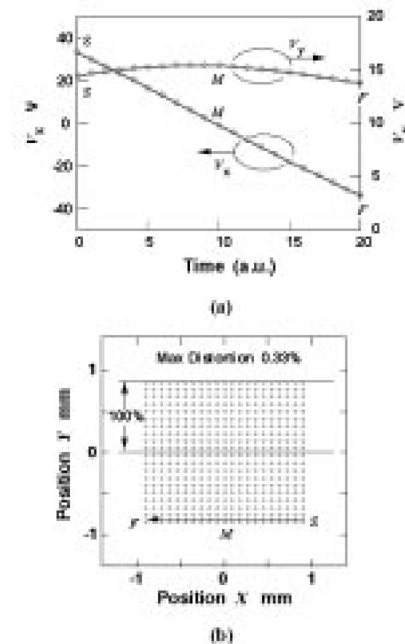

Fig. 15. Experimental results of scanning a perfect grid pattern. (a) Example of predistorted differential voltages V_x and V_y to scan a target line SF in Fig. 11(a). (b) Grid pattern obtained after calibration.

for scanning a horizontal line from point S to F in Fig. 11(a). Voltage V_x is calculated to be almost linear with time, since the calibration points on $\overline{SF}$ line up with a uniform step in the X-direction. On the other hand, voltage V_y is not a constant value but predistorted toward larger values around point M in order to compensate the calibration image [Fig. 11(a)], which distorts inwards around point M.

Fig. 15(b) plots the experimental result of grid scanning by this method. The spots on line $\overline{SF}$ are successfully scanned straight. Furthermore, the maximum distortion was found to be

as low as 0.33%. This minimal distortion is mostly attributed to the wobbling of the scanner, whose control voltages are changed stepwise. The maximum number of resolvable spots was measured to be 30 in the X_S-axis and 58 along the Y_S-axis. The difference is due to the diffraction from the surface topology of the mirror. The mirror quality (surface curvature and roughness) could be improved by using a thicker mirror that had been bonded on top of the polysilicon platform by a wafer-scale device transfer technique [19], [20].

Distortion obtained here is not small enough for applications such as free-space optical switches, which require sophisticated feedback control. For such application, therefore, the differential operation provides coarse positioning to swiftly reach the range of feedback. For other applications in which small distortion is not crucial, this technique is very useful to make a concise control system; for example, we have used the differential voltage operation for our confocal scanning microscope to successfully obtain images from a specimen [9].

VII. Conclusion

We have proposed three techniques to improve the scanning linearity of electrostatic micromechanical 2-D scanners: 1) using differential voltage operation, 2) optimizing the mirror shape, and 3) predistorting driving voltages after calibrating the scanner. Distortion of projected image has been dramatically improved from about 72% to 13% by using a pair of differential voltages over a bias voltage. Differential voltage operation has been found to suppress the crosstalk of two orthogonal scan axes. The results of differential operation could be well predicted by using the theoretical simulation presented in this paper. We used coordinate conversion matrices to model the electromechanical actuation of the 2-D scanner. By using the theoretical model, we found that a circular mirror had small distortion compared with a mirror of square or diamond-shape. A perfect grid pattern (0.33% distortion) was successfully scanned by predistorting the differential driving voltages after calibrating the transfer characteristics of the scanner. We believe that these techniques are very useful to improve the performance of optical MEMS applications based on 2-D scanners such as scanning displays, microscopes, free-space optical interconnections, and laser raders.

References

[1] P. M. Hagelin, U. Krishnamoorthy, C. M. Arft, J. P. Heritage, and O. Solgaard, "Scalable fiber optic switch using micromachined mirrors," in *Proc. 10th Int. Conf. Solid-State Sensors and Actuators (Transducers '99)*, Sendai, Japan, June 7–10, 1999, 2P6-2.

[2] D. T. Neilson *et al.*, "Fully provisioned 112 × 112 micro-mechanical optical crossconnect with 35.8 Tb/s demonstrated capacity," in *Proc. Tech. Digest Optical Fiber Comm. Conf. (OFC2000)*, Baltimore, ML, Mar. 7–10, 2000, PD12-1.

[3] S. Kurth, R. Hahn, C. Kaufmann, K. Kehr, J. Mehner, and U. Wollmann, "Silicon mirrors and micromirror arrays for spatial laser beam modulation," *Sensors Actuators A66*, pp. 76–82, 1998.

[4] H. Goto, "Two-dimensional micro-optical scanner excited by PZT thin film microactuator," *Proc. SPIE*, vol. 3419, pp. 227–235, 1998.

[5] M.-H. Kiang, O. Solgaard, K. Y. Lau, and R. Muller, "Polysilicon optical microscanners for laser scanning displays," *Sensors Actuators A70*, pp. 195–199, 1998.

[6] R. A. Conant, P. M. Hagelin, U. Krishnamoorthy, and O. Solgaard, "A raster-scanning full-motion video display using polysilicon micromachined mirrors," in *Proc. 10th Int. Conf. on Solid-State Sensors and Actuators (Transducers '99)*, Sendai, Japan, June 7–10, 1999, 2P3-2.

[7] A. Garnier, T. Bourouina, H. Fujita, E. Orsier, T. Masuzawa, T. Hiramoto, and J.-C. Peuzin, "A fast, robust and simple 2-D micro-optical scanner based on contactless magnetrostrictive actuation," in *Proc. IEEE 13th Int. Conf. on Micro Electro Mechanical Systems (MEMS 2000)*, Miyazaki, Japan, Jan. 23–27, 2000, pp. 715–720.

[8] D. L. Dickensheets and G. S. Kino, "Silicon-micromachined scanning confocal optical microscope," *J. Microelectromech. Syst.*, vol. 7, pp. 37–38, Mar. 1998.

[9] W. Piyawattanametha, H. Toshiyoshi, J. LaCosse, and M. C. Wu, "Surface-micromachined confocal scanning optical microscope," in *Proc. Lasers and Electro-Optics/Quantum Electronic and Laser Science Conference (CLEO/QELS 2000)*, San Francisco, CA, May 7–10, 2000, CThL3.

[10] W. Piyawattanametha, L. Fan, S.-S. Lee, G.-D. Su, and M.-C. Wu, "MEMS technology for optical crosslinks for micro/nano satellites," in *Proc. Int. Conf. on Integrated Nano/Microtechnology for Space Applications*, Houston, TX, Nov. 1–6, 1998.

[11] L. Fan, M. C. Wu, K. Choquette, and M. Crawford, "Self-assembled microactuated XYZ stages for optical scanning and alignment," in *Proc. 9th Int. Conf. on Solid-State Sensors and Actuators (Transducers '97)*, Chicago, IL, June 16–19, 1997, pp. 319–322.

[12] T. Akiyama, D. Collard, and H. Fujita, "Scratch drive actuator with mechanical links for self-assembly of three-dimensional MEMS," *J. Microelectromech. Syst.*, vol. 6, pp. 10–17, 1997.

[13] S. P. Timoshenko and J. N. Goodier, *Theory of Elasticity*, 3rd ed. New York: McGraw Hill, 1970.

[14] J.-Å. Schweiz and F. Ericson, "Evaluation of mechanical materials properties by means of surface micromachined structures," *Sensors Actuators A74*, pp. 1226–1330, 1999.

[15] J. M. Gere and S. P. Timoshenko, *Mechanics of Materials*, 4th ed. Boston: PWS, 1997.

[16] L.-S Fan, L. H. Lane, N. Robertson, L. Crawforth, M. A. Moser, T. C. Reiley, and W. Imaino, "W. Batch-fabricated milli-actuators," in *Proc. IEEE Micro Electro Mechanical Systems (MEMS '93)*, Fort Lauderdale, FL, Feb. 7–10, 1993, pp. 179–183.

[17] L.-S. Fan, S. J. Woodman, R. C. Moore, L. Crawforth, T. C. Reiley, and M. A. Moser, "Batch-fabricated area-efficient milli-actuator," in *Proc. 1994 Solid-State Sensor and Actuator Workshop*, Hilton Head, SC, June 13–16, 1994, pp. 38–42.

[18] K. Uchimaru, A. Kasahara, and M. Sekimura, U.S. Pat. 5 740 150, Apr. 14, 1998.

[19] G.-D. J. Su, H. Nguyen, P. Paterson, H. Toshiyoshi, and M. C. Wu, "Surface-micromachined 2D optical scanners with high-performance single-crystalline silicon micromirrors," in *Proc. 2000 Conf. on Lasers and Electro-Optics/Quantum Electronic and Laser Science (CLEO/QELS 2000)*, San Francisco, CA, May 7–10, 2000, Postdeadline paper CPD21-1.

[20] P. R. Patterson, G.-D. J. Su, H. Toshiyoshi, and M. C. Wu, "A MEMS 2-D scanner with bonded single-crystalline honeycomb micromirror," in *Proc. Solid-State Sensor and Actuator Workshop (Hilton Head 2000)*, Hilton Head Island, SC, June 4–8, 2000, Supplemental Digest of Late News Poster Session, pp. 17–18.

Hiroshi Toshiyoshi (M'97) received the M.Eng. and Ph.D. degrees in electrical engineering from the University of Tokyo, Tokyo, Japan, in 1993 and 1996, respectively.

Since 1996, he has been a Ph.D. Lecturer with the Institute of Industrial Science, the University of Tokyo. Since 1999, he has been a Visiting Assistant Professor at University of California, Los Angeles, for his sabbatical year. His research interest is MEMS for free-space optics.

Wibool Piyawattanametha was born in Bangkok, Thailand, in 1973. He received the B.Eng. degree from King Mongkut's Institute of Technology Ladkrabang (KMITL), Bangkok, in 1994 and the M.Sc. degree from the University of California, Los Angeles (UCLA) in 1999. He is currently pursuing the Ph.D. degree at UCLA.

From 1994 to 1997, he worked at Schlumberger Limited as a Field Engineer. His research interests include microelectromechanical systems (MEMS), biomedical imaging and sensing, and photonics.

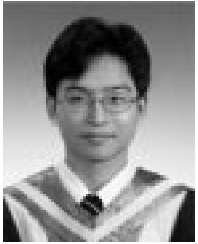

Cheng-Ta Chan was born in Tainan, Taiwan, R.O.C., on March 31, 1975. He received the B.S. degree in electrical engineering from Tatung University, Taiwan, in 1997 and the M.S. degree at National Chung Cheng University, Taiwan, in 1999. He is currently pursuing the Ph.D. degree at the Department of Electrical Engineering, National Chung Cheng University.

He is interested in digital signal processing and VLSI circuit design.

Ming C. Wu (M'99) received the M.S. and Ph.D. degrees in electrical engineering from the University of California, Berkeley, in 1985 and 1988, respectively.

From 1988 to 1992, he was Member of Technical Staff in AT&T Bell Laboratories, Murray Hill, NJ, where he conducted research in high speed semiconductor lasers and optoelectronics. In 1993, he joined the faculty of Electrical Engineering Department of University of California, Los Angeles (UCLA), and is currently Professor. His research interests include MEMS, MOEMS, and high-speed optoelectronics. He is Director of the MURI Center on RF Photonic Materials and Devices sponsored by ONR. He has published over 110 journal papers, 180 conference papers, contributed one book chapter, and holds 8 U.S. patents.

Dr. Wu was General Co-Chair for several Optical MEMS conferences, including IEEE LEOS Summer Topical Meeting on Optical MEMS in 1996 and 1998, and International Conference on Optical MEMS in 1999. He has also served on the Program Committees of IEEE MEMS Conference, OFC, CLEO, IEDM, and DRC. He received the Packard Foundation Fellowship in 1992, and the Meritorious Conference Paper Award of 1994 GOMAC. He is a member of the American Physical Society, Optical Society of America (OSA), URSI, and Eta Kappa Nu.